Scripta Materialia 130 (2017) 238–241

Contents lists available at ScienceDirect

Scripta Materialia

journal homepage: www.elsevier.com/locate/scriptamat

Regular article

Quantifying the three-dimensional damage and stress redistribution mechanisms of braided SiC/SiC composites by in situ volumetric digital image correlation

Brendan P. Croom [a], Peng Xu [b], Edward J. Lahoda [c], Christian P. Deck [d], Xiaodong Li [a,*]

[a] Department of Mechanical and Aerospace Engineering, University of Virginia, Room 342, 122 Engineer's Way, Charlottesville, VA 22904, USA
[b] Westinghouse Electric Company, 5801 Bluff Road, Hopkins, SC 29061, USA
[c] Westinghouse Electric Company, 1000 Westinghouse Drive, Suite 305, Cranberry Township, PA 16066, USA
[d] General Atomics, P.O. Box 85608, San Diego, CA 92186-5608, USA

ARTICLE INFO

Article history:
Received 2 November 2016
Received in revised form 12 December 2016
Accepted 13 December 2016
Available online xxxx

Keywords:
Ceramic matrix composites (CMC)
Three-dimensional tomography
Fracture
Digital image correlation

ABSTRACT

Coupled in situ micro-X-ray computed tomography and volumetric digital image correlation (V-DIC) strain measurements of expanding plug tests revealed the three-dimensional, microstructure-dependent mechanisms behind strain localization, damage initiation and stress redistribution in braided SiC/SiC composites. Hoop strain varied significantly through the composite thickness and was highest at regions of tow crossover; at higher loads, tow fracture initiated at these locations, and sample rupture propagated axially by connecting points of tow overlap. Finally, strain measurements after the failure of a tow on the interior surface quantified the three-dimensional stress redistribution mechanisms and damage tolerance of the SiC/SiC composite.

© 2016 Acta Materialia Inc. Published by Elsevier Ltd. All rights reserved.

While SiC fiber-reinforced, SiC matrix ceramic matrix composites (SiC/SiC CMCs) have attracted great interest for their superior strength and toughness at elevated temperatures, their intrinsically brittle constituents can fracture suddenly and unpredictably. The composite's mechanical behavior is strongly influenced by irregularities in the microstructure, including porosity, nonuniform tow-tow contact and variation in tow size, placement and orientation [1,2]. These defects often lead to failure initiation within the sample interior, which hinders direct observation and quantification of the damage mechanisms. Even in cases when failure initiates at a visible surface feature, full-field deformation measurements of the exterior surfaces (i.e., 3D digital image correlation; 3D-DIC) [3] are insufficient as the response still depends on the concealed, underlying structure. To unravel the complex failure mechanisms of CMCs, it is therefore desirable to obtain simultaneous three-dimensional strain and microstructural measurements of internal features before, during and after damage initiation.

Unfortunately, this is not feasible with conventional experimental approaches, so the effects of microstructural variation have been studied with "virtual experiments" using finite element simulations of experimentally-measured or statistically generated composite geometries [4,5]. Computational results are commonly compared to surface strain and damage maps obtained by 3D-DIC [3,4], but it remains unclear if the models accurately capture the internal behavior of *thick* composites, or for complex geometries with inaccessible surfaces. This concern is particularly valid for tubular nuclear cladding geometries, which commonly fail due to hoop stress on the internal surface. Therefore, new measurement techniques are required to truly validate virtual experiments.

Several test methods have been developed to evaluate the hoop strength of cylindrical samples, including internal pressurization via hydraulic fluid [6,7], or, more commonly, compression of an elastomeric insert in an "expanding plug" test [8,9]. Radial deformation u_r is typically measured on the external surface at select locations via dilatometer, which can be converted to hoop strain $\varepsilon_{\theta\theta}$ and hoop stress $\sigma_{\theta\theta}$ by the isotropic thick-walled cylinder equations,

$$u_r = \frac{P_i r}{E(r_o^2 - r_i^2)}\left[(1-\nu)r_i^2 + \frac{(1+\nu)r_i^2 r_o^2}{r^2}\right] \quad (1)$$

$$\varepsilon_{\theta\theta} = \frac{u_r}{r} \quad (2)$$

$$\sigma_{\theta\theta} = \frac{P_i}{r_o^2 - r_i^2}\left(r_i^2 + r_i^2 r_o^2 / r^2\right) \quad (3)$$

where r is the radial coordinate, r_i and r_o are the internal and outside radii of the cylinder, E and ν are the stiffness and Poisson's ratio of the cylinder, and P_i is the internal pressure. However, due to the *anisotropic*

* Corresponding author.
E-mail address: xl3p@virginia.edu (X. Li).

http://dx.doi.org/10.1016/j.scriptamat.2016.12.021
1359-6462/© 2016 Acta Materialia Inc. Published by Elsevier Ltd. All rights reserved.

mechanical properties and heterogeneous microstructure of SiC/SiC CMCs as well as small number of composite layers [10], it is unclear if the through-thickness deformation profile predicted by the *isotropic* thick-walled cylinder equations remains valid; this is a key question that can be answered with volumetric deformation measurements.

One promising technique is coupled in situ micro-X-ray Computed Tomography (μXCT) and Volumetric Digital Image Correlation (V-DIC) testing, which has been widely used to reveal with ~10 μm resolution the otherwise-inaccessible internal deformation/failure mechanisms of porous bone, foams and particle-reinforced composites [11–14]. Recent work by the authors have demonstrated that the contrast between fibers, pores and other microstructural features in dense fiber-reinforced polymer composites enables robust and highly sensitive V-DIC measurements of internal elasto-plastic deformation and microstructure-controlled buckling mechanisms [15]. The ability to correlate tomograms of polymer composites implies that similar measurement capabilities can be achieved for CMCs, especially in light of recent XCT measurements of microstructure and damage in SiC/SiC CMCs [16,17]. Indeed, coupled XCT/V-DIC techniques have recently been used as a benchmark for finite element simulations of deformation and damage in SiC/SiC CMCs [18,19].

In this work, coupled μXCT and V-DIC approaches are applied to in situ expanding plug tests of triaxially-braided SiC/SiC composite cladding tubes produced by a CVI process (provided by General Atomics). These specimens were in the as-fabricated condition (showing surface roughness caused by the underlying fiber architecture), and were not smoothed or polished. The composite specimens featured an axial height of 12.5 mm, an outer radius of 5.5 mm and a nominal wall thickness of 1.2 mm with 3 layers of braided tows. The fiber architecture was selected to provide similar strengths in axial and hoop directions, and resulted in a composite elastic modulus of 190 GPa in the hoop direction [7]. Using a custom loading stage (Fig. 1a), an incompressible Shore 95A polyurethane plug [20] was axially compressed within the sample to perform an expanding plug test; radial dilation of the plug loaded the interior surface of the specimen, contributing to deformation and failure by hoop stress.

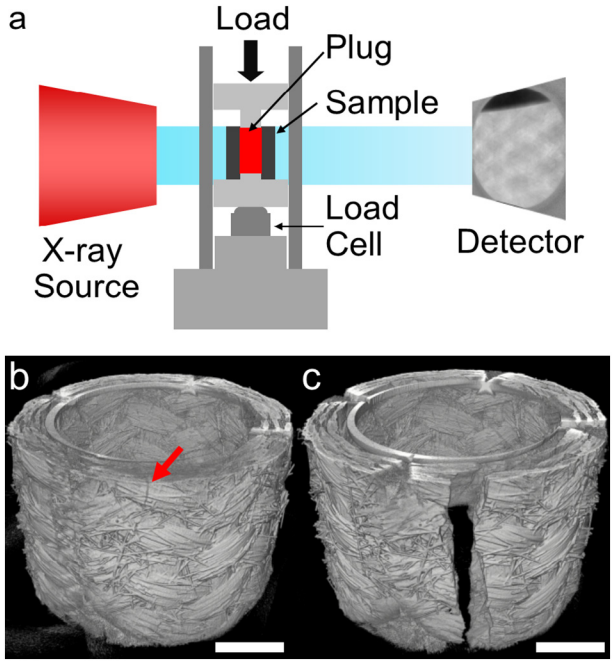

Fig. 1. Coupled μXCT and V-DIC setup. (a) Experimental apparatus, showing in situ expanding plug loading stage. (b–c) Representative in situ tomograms after (b) subcritical tow failure on exterior surface (highlighted by arrow) at 2400 N, and (c) after failure at 2630 N. The rubber plug and aluminum indenter are hidden to show interior composite microstructure. Scale bars in (b–c): 3 mm.

Tomograms with 500 × 500 × 500 voxels and voxel resolution of 15.6 μm were acquired throughout the deformation of four composite samples (XRadia MicroXCT-200). While the field of view for each scan was only 7.8 mm in diameter, overlapping XCT scans recorded the mechanical response of the entire specimen at each load increment (Fig. 1b–c). Representative in situ reconstructions are shown in Fig. 1b–c after failure of a single tow at 2400 N and after specimen fracture at 2630 N, which clearly illustrate prominent microstructural features such as tow geometry and large voids (>50 μm), as well as matrix microcracks and fracture surfaces. Tomograms were smoothed with a 3D Gaussian filter before correlation with commercial V-DIC software (Vic-Volume, Correlated Solutions), which removed noise and has been shown to improve image correlation accuracy [21,22]. In this way, the volumetric mechanical response and damage mechanisms (e.g., matrix microcracking, tow failure, etc.) could be related to the underlying composite microstructure, and key questions about (1) the validity of homogeneous thick-wall cylinder elasticity assumptions, (2) tow failure mechanisms, and (3) stress redistribution could be answered.

Representative V-DIC results are presented in Fig. 2, which shows the hoop stress on the *interior* and *exterior* surfaces of the composite at various loads before specimen fracture at 2950 N. Evidenced by prominent strain concentrations, it is clear that mechanical response is strongly regulated by microstructure. In the pre-damage loading regime up to 2500 N, we observed localized strain concentrations of $\varepsilon_{\theta\theta} = 0.25 - 0.35\%$ that corresponded to tow crossovers on both the interior and exterior surfaces. These regions naturally exhibit the highest stress/strain response, as they distribute load between overlapping tows [23]. Strain away from contact regions was somewhat lower, $\varepsilon_{\theta\theta} = 0.15\%$, and even negative at some locations; highly heterogeneous and locally negative strains have been observed in both surface DIC measurements and associated finite element simulations of stochastic woven CMCs, and are attributed to microstructural variation and defects [24]. Some strain concentrations on the interior surface (one of which is marked by inset in Fig. 2c) were proximate to the location of tow failure at 2700 N, potentially indicating that failure initiated from these inter-tow contacts.

The hoop strain distributions on the interior and exterior surfaces were not strongly related; that is, the regions with highest deformation varied through the thickness. Rather, the location of strain concentrations was governed by the immediate tow architecture rather than more distant microstructural features. This was particularly true in the elastic loading regime before microstructural damage, as inferred from strain maps at 2100 and 2500 N (b and c in Fig. 2). A notable exception to this trend occurred after tow failure on the interior surface, which produced a large stress redistribution to tows on the exterior surface (Fig. 2d). Therefore, surface strain measurements were only indicative of large interior damage but were not sensitive to elastic strains on the interior surface.

Comparison of the interior and exterior strain profiles revealed that the interior surface displayed several minor hoop strain peaks away from tow-contact regions, but these were not apparent on the exterior surface. This was probably caused by boundary conditions imposed by the expanding plug. For instance, variation in local plug-composite contact stress as the elastomer conformed to the interior surface could produce highly three-dimensional and irregular loading conditions. Local loading effects were dissipated through the composite thickness via St. Venant's principle, resulting in a "cleaner" strain distribution that only showed strain concentrations at inter-tow contacts. It is possible that grinding of the interior surface to remove tow roughness or the addition of an inner monolithic SiC layer could produce a more uniform stress distribution.

Although it was clear that the microstructure contributed to elevated strains at the tow overlaps, why did failure initiate at the particular location? How did failure propagate from the damaged tow? Detailed inspection of the tow architecture in Fig. 3 identified a large inter-tow

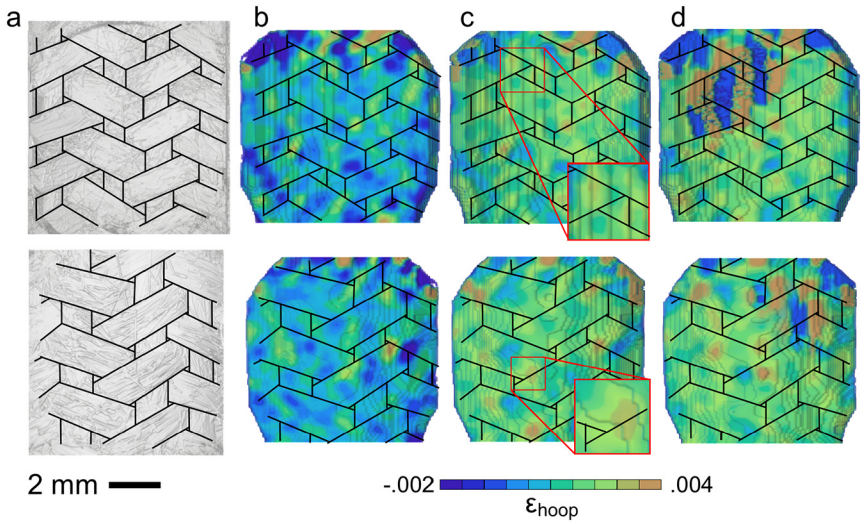

Fig. 2. V-DIC computed hoop strain $\varepsilon_{\theta\theta}$ on interior (top) and exterior (bottom) surface. (a) Tomogram at 0 N load, with tows outlined in black. (b–d) $\varepsilon_{\theta\theta}$ measurements acquired within the elastic regime at (b) 2100 N and (c) 2500 N, and (d) after interior tow failure at 2730 N, which appears as levels of high strain. The specimen failed completely at 2950 N. Prominent strain concentrations at 2500 N are highlighted by inset.

spacing of 0.86 mm at the point of failure initiation, which was 25–60% larger than in similar regions. Based on this, we could expect an increased length of biased tow that was not supported by underlying material. The radial pressure exerted by the elastomeric plug resulted in the maximum bending moment at the tow overlap, analogous to the stress distribution on a cantilever beam (Fig. 3b). In this scenario, the maximum principal stress – the relevant failure criteria for brittle SiC constituents – would occur at the root of the biased tow, which was indeed where tow failure occurred. This natural stress concentration was enhanced by the increased unsupported length and by load transfer at the tow contacts. Although the small specimen size restricted the number of tow-spacing measurements, these results suggested that tow spacing must be tightly controlled to produce a uniform mechanical response. Further experiments are required to quantify the specific contribution of tow spacing to failure compared to other defects such as porosity, tow misorientation and variable matrix thickness.

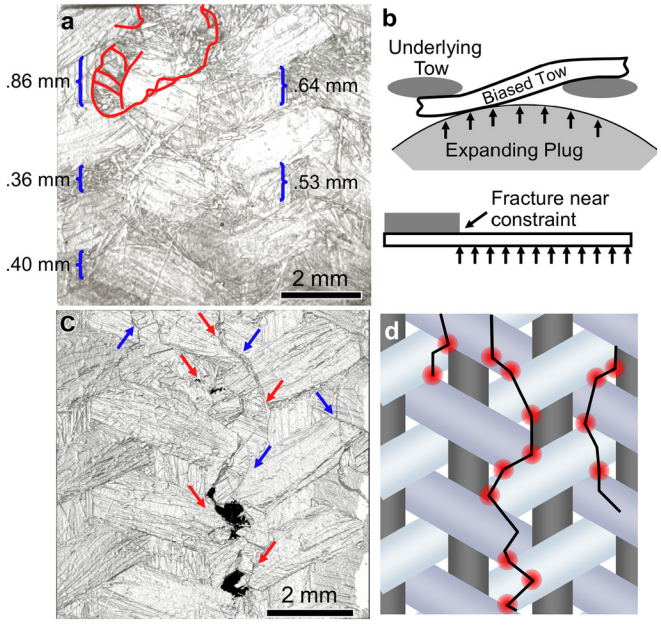

Fig. 3. Tow failure is regulated by microstructural variation. (a) Measurements of inter-tow spacing. The tow fracture pattern (evident as region of large hoop strain in Fig. 2) is traced in red for clarity. (b) Schematic of biased tow failure mechanism. (c) Fracture pattern on interior surface (different specimen), showing biased tow failure at overlap with axial tows (red arrows) and other biased tows (blue arrows). (d) Schematic of fracture and microcrack paths visible in (c), showing alignment with tow overlaps (highlighted in red). (For interpretation of the references to color in this figure legend, the reader is referred to the web version of this article.)

Analysis of the fracture surface of a *different* specimen (Fig. 3c) confirmed that this fracture mechanism prevailed along the entire interior surface. The jagged fracture path along the interior surface connected nearly all points of contact with underlying axial or biased tows (Fig. 3d). In each of the four samples, the fracture path was constrained between two axial tows, and the cracks never bridged an axial tow on the interior surface to propagate laterally; this indicated that the axial tows fully arrested and/or deflected the propagating cracks, and that failure was dominated by hoop stress. In addition, the fractured samples exhibited microcracks parallel to the final fracture surface (Fig. 3c–d) with similar crack deflection characteristics. While it could not be confirmed whether these cracks formed before, during or after sample rupture, SEM and XCT measurements revealed that the supplemental microcracks only appeared within 3 mm of the final fracture surface, suggesting that their initiation was closely related to the fracture process. Therefore, it was believed that the elevated hoop stresses that contributed to sample rupture also created parallel microcracks through a crack bridging mechanism.

With new insight into the mechanisms of subcritical tow failure, we now seek to understand the redistribution of stress around damaged regions. The damage observed in Fig. 3 was constrained to the interior layer, leaving two intact layers of load-bearing tows outside the damaged region. Analysis of the hoop strain in two regions before and after tow fracture revealed complex deformation and nonuniform stress redistribution behavior (Fig. 4). Before tow fracture, the average strain in regions "b" and "c" at 2100 N closely resembled the theoretical profile predicted by Eqs. (1–3) (dashed line in Fig. 4b–c), yet the two regions demonstrated unique variations in hoop strain on the interior surface. At 2100 N, region "b" exhibited a range from $\varepsilon_{\theta\theta}^{2.5\%} = 0.02\%$ to $\varepsilon_{\theta\theta}^{97.5\%} = 0.23\%$ (strains at 2.5th and 97.5th percentiles) on the interior surface, compared to a range of $\varepsilon_{\theta\theta}^{2.5\%} = -0.10\%$ to $\varepsilon_{\theta\theta}^{97.5\%} = 0.35\%$ in region "c". The large variation in region "c" was indicative of widespread microcracking, as crack opening displacements would create large pseudo-strains and simultaneously unload adjacent material to create small strains.

After tow fracture at 2730 N, the hoop strain evolved differently in the two regions, supporting a conclusion of anisotropic stress redistribution. In both regions, the average (through-thickness) hoop strain increased to a value of $\varepsilon_{\theta\theta}^{avg} = 0.163\%$, which constituted a relatively larger

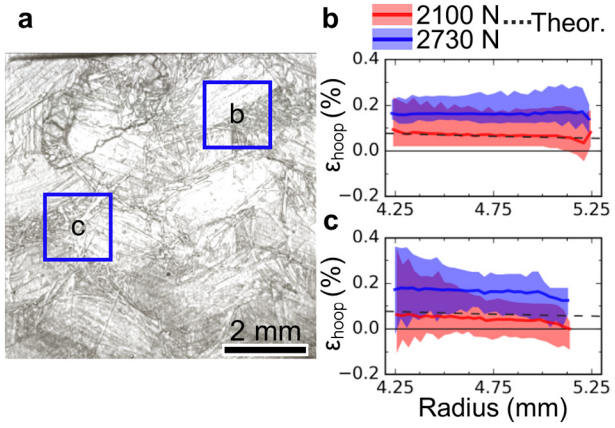

Fig. 4. Stress redistribution associated with tow failure. (a) Tomogram of specimen 4 after failure of interior tow. (b–c) V-DIC measured through-thickness hoop strain at loads before and after tow failure corresponding to regions (b) to right and (c) beneath failed tow. Dark colored lines represent mean strain response, while colored bands encapsulate 95% of strain measurements. Data is compared to theoretical hoop strain at 2100 N via thick-wall cylinder equations (dashed line). Radial thicknesses of the two regions are different due to microstructural variation. (For interpretation of the references to color in this figure legend, the reader is referred to the web version of this article.)

increase in region "c" than in region "b" and suggested that stress was preferentially redistributed axially rather than radially. The average strain increased uniformly through the thickness in region "c", which maintained a deformation gradient consistent with Eqs. (1–3). In contrast, the average strain increased preferentially on the outside of region "b", resulting in a uniform strain distribution that varied little with radial position. As a result, both the average and maximum values of $\varepsilon_{\theta\theta}$ on the interior surface were higher in region "c" than in region "b", and these values in region "c" approached the critical fracture strain for individual tows [25]. Subsequent loading to 2950 N resulted in fracture propagation along the axial direction, consistent with this analysis.

In conclusion, coupled XCT/V-DIC measurements of in situ expanding plug tests provided unprecedented access to the internal deformation and failure mechanisms of SiC/SiC composites. This new experimental technique achieved quantitative tow-level strain measurements, which were cross-referenced to high-resolution 3D microstructural images to elucidate the processing-microstructure-deformation-failure relationships of as-fabricated braided SiC/SiC composites. These measurements revealed key differences between internal and external deformation trends, and found that surface-based measurements only rarely corresponded to internal strain distributions. Rather, the strain distribution and failure of the braided composite was most strongly predicted by the local tow architecture. Comparison between strain distributions, composite microstructure and failure mechanisms confirmed that large local tow spacing increased peak strain at adjacent inter-tow contacts and facilitated composite failure, which implies that tight control of tow alignment is necessary for good composite-level mechanical properties. These novel measurements revealed that tow failure at inter-tow contacts was the primary damage mechanism for this particular braided tow architecture, which was facilitated by load transfer between tows and stress distributions analogous to cantilever beams. Based on these measurements, tow spacing is believed to strongly influence the failure properties of braided SiC/SiC composites.

Finally, the current technique provides meaningful one-to-one comparison for FE simulations of statistically-generated composite models, and is therefore anticipated to be an essential tool for model validation. The coupled XCT/V-DIC approach successfully captured the nonlinear deformation, damage, stress redistribution and failure characteristics of braided CMCs, which is the central objective of virtual experiments. Since tow failure initiated on the sample interior, and V-DIC measurements suggested that exterior measurements were not sensitive to *internal deformation and damage*, these results prove that surface-based measurements (as from 3D-DIC, etc.) are insufficient experimental benchmarks for the simulations. Although results were only demonstrated for four samples, and further testing is required to assess the robustness of V-DIC measurements, the results indicate that three-dimensional XCT-based measurements are suitable and essential to validate FE models for thick, multi-ply composites.

Acknowledgements

This material is based upon work supported by Westinghouse Electric Company. BPC was supported by the National Science Foundation (NSF) Graduate Research Fellowship Program under Grant No. 1315231. We thank General Atomics (contact: Dr. Christian P. Deck) for generously providing the specimens used in this work.

References

[1] H. Bale, M. Blacklock, M.R. Begley, D.B. Marshall, B.N. Cox, R.O. Ritchie, J. Am. Ceram. Soc. 95 (2012) 392–402.
[2] M.N. Rossol, T. Fast, D.B. Marshall, B.N. Cox, F.W. Zok, J. Am. Ceram. Soc. 98 (2015) 205–213.
[3] V.P. Rajan, M.N. Rossol, F.W. Zok, Exp. Mech. 52 (2012) 1407–1421.
[4] B.N. Cox, H.A. Bale, M. Begley, M. Blacklock, B.-C. Do, T. Fast, M. Naderi, M. Novak, V.P. Rajan, R.G. Rinaldi, R.O. Ritchie, M.N. Rossol, J.H. Shaw, O. Sudre, Q. Yang, F.W. Zok, D.B. Marshall, Annu. Rev. Mater. Res. 44 (2014) 479–529.
[5] R.G. Rinaldi, M. Blacklock, H. Bale, M.R. Begley, B.N. Cox, J. Mech. Phys. Solids 60 (2012) 1561–1581.
[6] K. Mosley, Arch. Proc. Inst. Mech. Eng. vol. 1–196 (196) (1982) 1847–1982 (123–139).
[7] L.H. Alva, X. Huang, G.M. Jacobsen, C.A. Back, in: H. Jin, C. Sciammarella, S. Yoshida, L. Lamberti (Eds.), Adv. Opt. Methods Exp. Mech. Vol. 3 Proc. 2014 Annu. Conf. Exp. Appl. Mech, Springer International Publishing 2015, pp. 387–393.
[8] T.S. Byun, E. Lara-Curzio, R.A. Lowden, L.L. Snead, Y. Katoh, J. Nucl. Mater. 367–370 (A) (2007) 653–658.
[9] H. Jiang, J.A.J. Wang, J. Nucl. Mater. 446 (2014) 27–37.
[10] Q.D. Yang, K.L. Rugg, B.N. Cox, D.B. Marshall, J. Am. Ceram. Soc. 88 (2005) 719–725.
[11] J.Y. Buffiere, E. Maire, J. Adrien, J.P. Masse, E. Boller, Proc. Soc. Exp. Mech. Inc. 67 (2010) 289–305.
[12] E. Maire, P.J. Withers, Int. Mater. Rev. 59 (2014) 1–43.
[13] B.K. Bay, T.S. Smith, D.P. Fyhrie, M. Saad, Exp. Mech. 39 (1999) 217–226.
[14] E. Verhulp, B. van Rietbergen, R. Huiskes, J. Biomech. 37 (2004) 1313–1320.
[15] B. Croom, W.-M. Wang, J. Li, X. Li, Exp. Mech. 56 (2016) 999–1016.
[16] H.A. Bale, A. Haboub, A.A. MacDowell, J.R. Nasiatka, D.Y. Parkinson, B.N. Cox, D.B. Marshall, R.O. Ritchie, Nat. Mater. 12 (2012) 40–46.
[17] D. Frazer, M.D. Abad, D. Krumwiede, C.A. Back, H.E. Khalifa, C.P. Deck, P. Hosemann, Compos. Part A Appl. Sci. Manuf. 70 (2015) 93–101.
[18] L. Saucedo-Mora, T.J. Marrow, Philos. Trans. R. Soc. London A Math. Phys. Eng. Sci. 374 (2016).
[19] L. Saucedo-Mora, M. Mostafavi, D. Khoshkhou, C. Reinhard, R. Atwood, S. Zhao, B. Connolly, T.J. Marrow, Finite Elem. Anal. Des. 110 (2016) 11–19.
[20] G.M. Jacobsen, J.D. Stone, H.E. Khalifa, C.P. Deck, C.A. Back, J. Nucl. Mater. 452 (2014) 125–132.
[21] B. Pan, Opt. Lasers Eng. 51 (2013) 1161–1167.
[22] P. Mazzoleni, F. Matta, E. Zappa, M.A. Sutton, A. Cigada, Opt. Lasers Eng. 66 (2015) 19–33.
[23] M.N. Rossol, V.P. Rajan, F.W. Zok, Compos. Part A Appl. Sci. Manuf. 74 (2015) 141–152.
[24] M. Blacklock, J.H. Shaw, F.W. Zok, B.N. Cox, Compos. Part A Appl. Sci. Manuf. 85 (2016) 40–51.
[25] C. Chateau, L. Gélébart, M. Bornert, J. Crépin, D. Caldemaison, C. Sauder, J. Mech. Phys. Solids 63 (2014) 298–319.